Inorg. Chem. **2001,** *40,* 157−164

Photon Upconversion Properties of Ni^{2+} in Magnetic and Nonmagnetic Chloride Host Lattices

Oliver S. Wenger and Hans U. Güdel*

Departement für Chemie und Biochemie, Universität Bern, Freiestrasse 3, CH-3000 Bern 9, Switzerland

Received June 19, 2000

Near-infrared to visible upconversion luminescence in Ni^{2+}:$CsCdCl_3$, Ni^{2+}:$CsMnCl_3$, and Ni^{2+}:$RbMnCl_3$ is presented and analyzed. In all three materials upconversion occurs via a sequence of ground-state absorption/excited-state absorption processes, which are both formally spin-forbidden transitions. Consequently, in the diamagnetic Ni^{2+}:$CsCdCl_3$ they are weak, and the efficiency of the upconversion process is relatively low. This is in clear contrast to the isostructural Ni^{2+}:$RbMnCl_3$ where the spin selection rule relaxes because of $Ni^{2+}-Mn^{2+}$ exchange interactions, leading to an intensity enhancement of the spin−flip transitions involved in the Ni^{2+} upconversion mechanism. This results in an exchange-induced enhancement of the upconversion rate in Ni^{2+}:$RbMnCl_3$ relative to Ni^{2+}:$CsCdCl_3$ by 2 orders of magnitude after two-color excitation into the maxima of the ground-state and excited-state absorption bands. In Ni^{2+}:$CsMnCl_3$ the $Ni^{2+}-Mn^{2+}$ exchange interaction does not play a significant role. This is due to the different $Ni^{2+}-Cl^{-}-Mn^{2+}$ bridging geometry relative to Ni^{2+}:$RbMnCl_3$. In contrast to Ni^{2+}:$CsCdCl_3$ and Ni^{2+}:$RbMnCl_3$ where the upconversion luminescence occurs from Ni^{2+}, in Ni^{2+}:$CsMnCl_3$ the upconverted energy is emitted from Mn^{2+} in the visible spectral region. This leads to an enhanced *visible* upconversion luminescence in Ni^{2+}:$CsMnCl_3$, relative to the other two samples where Ni^{2+} near-infrared inter-excited-state emissions compete with the visible upconversion luminescence.

1. Introduction

Many studies have been made over the past few years on materials displaying new photophysical effects. Among those, the photon upconversion process[1,2] has received a lot of attention. Photoexcitation at long wavelengths is followed by short wavelength luminescence. A defining characteristic for all upconversion materials is the existence of a long-lived intermediate state that serves as a storage reservoir for the pump energy. Therefore, the basic prerequisite for upconversion materials is the existence of at least two emitting states. Because of the shielded nature of the spectroscopically active 4f and 5f orbitals, luminescence from multiple excited states is a common phenomenon in rare earth doped insulating materials. Thus, the vast majority of upconversion studies has been devoted to lanthanide systems. Such materials have found use, for example, as laser light sources,[3] imaging materials,[4] and IR quantum counters.[5] By contrast, very few studies exist on transition metal ion upconversion systems. This is mainly due to the fact that the electron−phonon interaction of these ions is much stronger than in the case of the rare earths. Consequently, most transition metal ions follow Kasha's rule[6] and have at most one metastable excited state with a sufficently long lifetime to observe luminescence, i.e., the first excited state. Among transition metal ions in octahedral coordination, upconversion has so far only been observed in Ti^{2+},[7] Ni^{2+},[8,9] Mo^{3+},[10] Re^{4+},[10,11] and Os^{4+}.[12,13] The great advantage of such transition metal upconverters compared to rare earth upconversion ions is their sensitivity toward their ligand field environments. It allows a tuning of the upconversion properties by means of chemical variation. It is this fact that we exploit in this study.

Ni^{2+} upconversion has been observed in oxides,[9] fluorides,[9] and chlorides.[8] The upconversion efficiency of the Ni^{2+} ion is, particularly in chlorides, limited by the fact that two weak spin-forbidden transitions are involved in the upconversion process. In this paper we show how the Ni^{2+} spin selection rule relaxes in the presence of $Ni^{2+}-Mn^{2+}$ exchange interaction and we report the influence of such a magnetic perturbation on the Ni^{2+} upconversion properties. For that purpose we compare the upconversion properties of Ni^{2+}:$CsCdCl_3$ and isostructural Ni^{2+}:$RbMnCl_3$. The comparison with Ni^{2+}:$CsMnCl_3$ underlines the importance of the exact $Ni^{2+}-Mn^{2+}$ exchange pathway. In addition, we demonstrate that in Ni^{2+}:$CsMnCl_3$ the *visible* upconversion luminescence output is enhanced relative to Ni^{2+}:$CsCdCl_3$.

2. Crystal and Magnetic Structures

The local environments of the divalent cations are quite similar in $CsMnCl_3$, $RbMnCl_3$, and $CsCdCl_3$ and consist of

---

[1] Wright, J. C. In *Topics in Applied Physics: Radiationless Processes in Molecules and Condensed Phases*; Fong, F. K., Ed.; Springer: Berlin, 1976; pp 239−295.
[2] Auzel, F. E. *Proc. IEEE* **1973**, *61*, 758−786.
[3] Lenth, W.; Macfarlane, R. M. *Opt. Photonics News* **1992**, *3*, 8−15.
[4] Downing, E.; Hesselink, L.; Ralston, J.; Macfarlane, R. *Science* **1996**, *273*, 1185−1189.
[5] Chivian, J. S.; Case, W. E.; Eden, D. D. *Appl. Phys. Lett.* **1979**, *35*, 124−125.
[6] Kasha, M. *Discuss. Faraday Soc.* **1950**, *9*, 14−19.
[7] Jacobsen, S. M.; Güdel, H. U. *J. Lumin.* **1989**, *43*, 125−137.
[8] Oetliker, U.; Riley, M. J.; May, P. S.; Güdel, H. U. *Coord. Chem. Rev.* **1991**, *111*, 125−130 and references therein.
[9] Moncorgé, R.; Benyattou, T. *Phys. Rev. B* **1988**, *37*, 9186−9196.
[10] Gamelin, D. R.; Güdel, H. U. *J. Am. Chem. Soc.* **1998**, *120*, 12143−12144.
[11] Gamelin, D. R.; Güdel, H. U. *Inorg. Chem.* **1999**, *38*, 5154−5164.
[12] Wermuth, M.; Güdel, H. U. *Chem. Phys. Lett.* **1998**, *281*, 81−85.
[13] Wermuth, M.; Güdel, H. U. *J. Am. Chem. Soc.* **1999**, *121*, 10102−10111.

10.1021/ic000662p CCC: $20.00

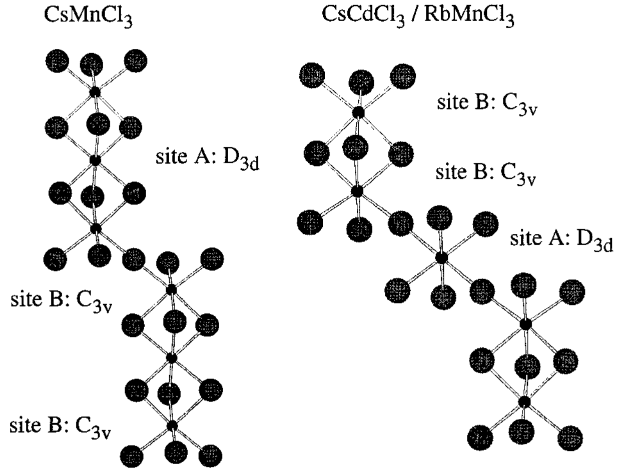

Figure 1. Relevant elements of the $CsMnCl_3$ and $RbMnCl_3/CsCdCl_3$ crystal structures illustrating the two types of Mn^{2+}/Cd^{2+} sites D_{3d} (A) and C_{3v} (B) as well as the bridging arrangements (face- and corner-sharing octahedra).

trigonally distorted $[M^{II}Cl_6]^{4-}$ octahedra. The Ni^{2+} dopant ions substitute for Mn^{2+} and Cd^{2+}.

$CsMnCl_3$ crystallizes in the hexagonal space group $R\bar{3}m$.[14] The compound consists of face-sharing trimers of $[MnCl_6]^{4-}$ octahedra. Each trimer is linked to six other trimers by shared corners. This is illustrated in Figure 1 on the left. We see the two crystallographically nonequivalent sites A and B with D_{3d} and C_{3v} point symmetries, respectively.

$RbMnCl_3$ and $CsCdCl_3$ are isostructural and crystallize in the hexagonal space group $P6_3/mmc$.[15,16] Two-thirds of the $[M^{II}Cl_6]^{4-}$ octahedra form dimers by sharing one face. The site symmetry of these M^{II} ions is C_{3v}. These $[M^{II}{}_2Cl_9]^{5-}$ units share corners with six $[M^{II}Cl_6]^{4-}$ with D_{3d} point symmetry. This is illustrated in Figure 1 on the right. EPR investigations of 0.1% Ni^{2+}:$CsCdCl_3$[16] indicate that Ni^{2+} substitutes into only one of the two Cd^{2+} sites, and in an optical spectroscopic study this was identified as the C_{3v} site.[17] We assume that this is also the case in the isostructural $RbMnCl_3$. It is also reasonable to assume that in $CsMnCl_3$ the Ni^{2+} dopant ions preferentially substitute into only one of the two distinct Mn^{2+} sites.

Both $CsMnCl_3$ and $RbMnCl_3$ are three-dimensional antiferromagnets with ordering temperatures of 67 and 94 K, respectively.[18,19] In both materials the spin orientation is perpendicular to the crystallographic *c* axis.

3. Experimental Section

The methods of sample preparation and crystal growth used to obtain the crystals for these investigations have been described elsewhere.[20,21] The Ni^{2+} dopant concentrations in the crystals used for the spectroscopic measurements were 0.1%/10% in $CsCdCl_3$ and 10% in $CsMnCl_3$/$RbMnCl_3$. In all crystals the nominal and effective dopant concentrations were found to be almost identical.

Absorption spectra were measured on a Cary 5e (Varian) spectrometer. Continuous-wave downconversion luminescence measurements were performed using an Ar^+ laser (Ion Laser Technology) or a Kr^+ laser (Coherent Innova 300) as an excitation source. The sample luminescence was dispersed by a $^3/_4$ m single monochromator (Spex 1702). Visible luminescence was detected using a cooled red sensitive photomultiplier tube (Hamamatsu 3310-01) connected to a photon-counting system (Stanford Research 400). Near-infrared luminescence was detected with a low-noise Ge detector (ADC 403L, operated at 77 K) or a dry-ice-cooled PbS detector (Hamamatsu P3337) and processed with a lock-in amplifier (Stanford Research 510). For upconversion luminescence and excitation measurements two Ar^+ laser (Spectra Physics 2060-10A) pumped Ti:sapphire lasers (Spectra Physics 3900S) were used. The detection system consisted of a 0.85 m double monochromator and a cooled photomultiplier tube (RCA 31034) connected to the photon-counting system (SR400).

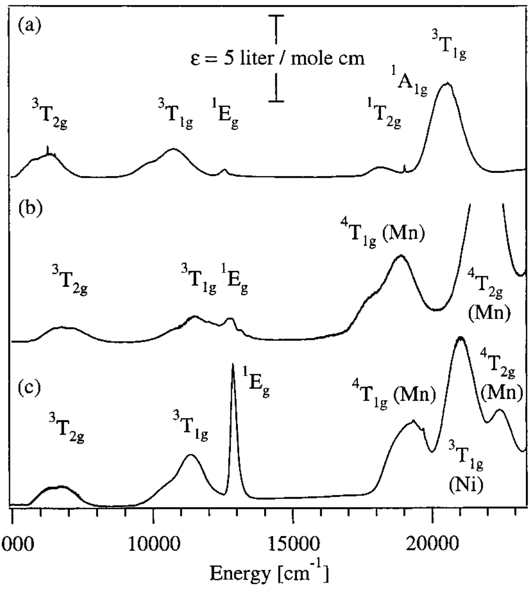

Figure 2. The 15 K survey absorption spectra of (a) 10% Ni^{2+}:$CsCdCl_3$ (axial), (b) 10% Ni^{2+}:$CsMnCl_3$ (unpolarized), and (c) 10% Ni^{2+}:$RbMnCl_3$ (axial). Spin singlet and triplet labels denote Ni^{2+} absorption bands, and spin quartet labels indicate Mn^{2+} absorptions.

Rectangular excitation pulses for the lifetime experiments were generated by passing the laser beam through an accousto-optic modulator (Coherent 305) connected to a function generator (Stanford Research DS345). The sample luminescence decay was analyzed with a multichannel scaler (Stanford Research 430).

Sample cooling was achieved by a closed-cycle cryostat (Air Products Displex) for absorption measurements and with a He gas flow technique for the emission experiments.

All luminescence spectra were corrected for the sensitivity of the detection system and are displayed as photon counts versus energy.

4. Results

Spectra a, b, and c of Figure 2 shows the survey absorption of 10% Ni^{2+}-doped $CsCdCl_3$, $CsMnCl_3$, and $RbMnCl_3$, respectively. The absorption spectrum of Ni^{2+} in the near-infrared and visible spectral region consists of three spin-allowed and three spin-forbidden d−d transitions as shown in Figure 2a. In the Ni^{2+}:$CsMnCl_3$ and Ni^{2+}:$RbMnCl_3$ absorption spectra the two lowest energy $^4T_{1g}$ and $^4T_{2g}$ absorption bands of Mn^{2+} are superimposed on the $^1T_{2g}$, $^1A_{1g}$, and $^3T_{1g}$ (^3P) absorption bands of Ni^{2+}. Below 17 000 cm^{-1} Mn^{2+} is spectroscopically transparent. Relative to 10% Ni^{2+}:$CsCdCl_3$ the integrated $^3A_{2g} \rightarrow {}^1E_g$ absorption intensity is larger in 10% Ni^{2+}:$CsMnCl_3$ and 10% Ni^{2+}:$RbMnCl_3$ by factors of 5 and 20, respectively.

In Figure 3 lifetimes of the $^3T_{2g}$ first excited state of 0.1% Ni^{2+}:$CsCdCl_3$ (circles), 10% Ni^{2+}:$CsMnCl_3$ (triangles), and 10% Ni^{2+}:$RbMnCl_3$ (squares) are plotted as a function of temperature. The $^3T_{2g}$ lifetimes were extracted from the rise times in the

---

(14) Ting-I, L.; Stucky, G. D.; McPherson, G. L. *Acta Crystallogr.* **1973**, *B29*, 1330−1335.

(15) Goodyear, J.; Steigman, G. A.; Ali, M. E. *Acta Crystallogr.* **1977**, *B33*, 256−258.

(16) Chang, J. R.; McPherson, G. L.; Atwood, J. L. *Inorg. Chem.* **1975**, *14*, 3079−3085.

(17) Oetliker, U.; Riley, M. J.; Güdel, H. U. *J. Lumin.* **1995**, *63*, 63−73.

(18) Melamud, M.; Makovsky, J.; Shaked, H. *Phys. Rev. B* **1971**, *3*, 3873.

(19) Melamud, M.; Makovsky, J.; Shaked, H.; Shtrikman, S. *Phys. Rev. B* **1971**, *3*, 821−826.

(20) May, P. S.; Güdel, H. U. *J. Lumin.* **1989**, *46*, 277−290.

(21) Kambli, U.; Güdel, H. U. *J. Phys. C* **1984**, *17*, 4041−4054.

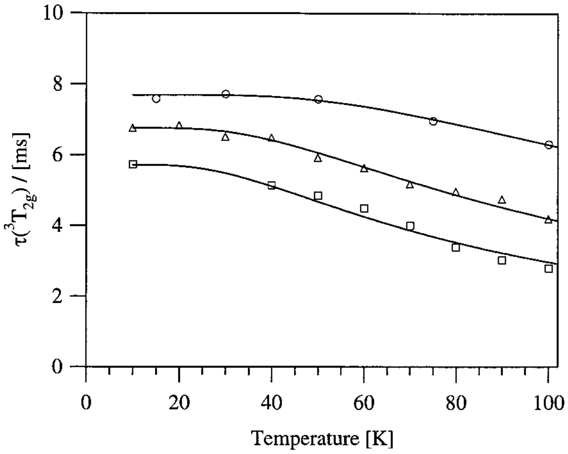

Figure 3. Temperature dependences of the Ni^{2+} $^3T_{2g}$ lifetimes in 0.1% Ni^{2+}:$CsCdCl_3$ (circles), 10% Ni^{2+}:$CsMnCl_3$ (triangles), and 10% Ni^{2+}:$RbMnCl_3$ (squares). The solid lines are fits of eq 1 to the experimental data.

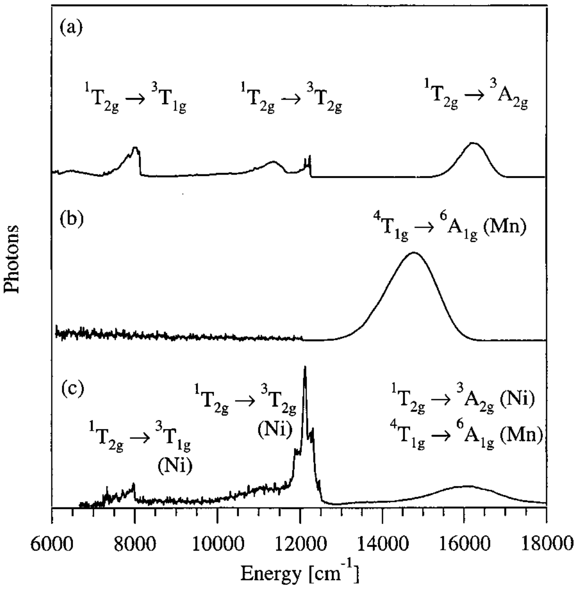

Figure 4. The 15 K unpolarized survey luminescence spectra of (a) 10% Ni^{2+}:$CsCdCl_3$ (excited at 20 492 cm^{-1}), (b) 10% Ni^{2+}:$CsMnCl_3$ (excited at 17 599 cm^{-1}), and (c) 10% Ni^{2+}:$RbMnCl_3$ (excited at 20 986 cm^{-1}). Spectra a and c are scaled to an equal integrated $^1T_{2g} \rightarrow {}^3A_{2g}$ emission intensity.

upconversion luminescence transients obtained after low-power near-infrared excitation with rectangular square wave pulses.

The 15 K unpolarized survey luminescence of 10% Ni^{2+}:$CsCdCl_3$, 10% Ni^{2+}:$CsMnCl_3$, and 10% Ni^{2+}:$RbMnCl_3$ are presented in spectra a, b, and c of Figure 4, respectively. Spectra a and c are scaled to an equal integrated $^1T_{2g} \rightarrow {}^3A_{2g}$ emission intensity. Ni^{2+}:$CsCdCl_3$ and Ni^{2+}:$RbMnCl_3$ were excited into the Ni^{2+} $^3T_{1g}$ (^3P) absorption band at 20 492 and 20 986 cm^{-1}, respectively. Ni^{2+}:$CsMnCl_3$ was excited into the Mn^{2+} $^4T_{1g}$ absorption band at 17 599 cm^{-1}.

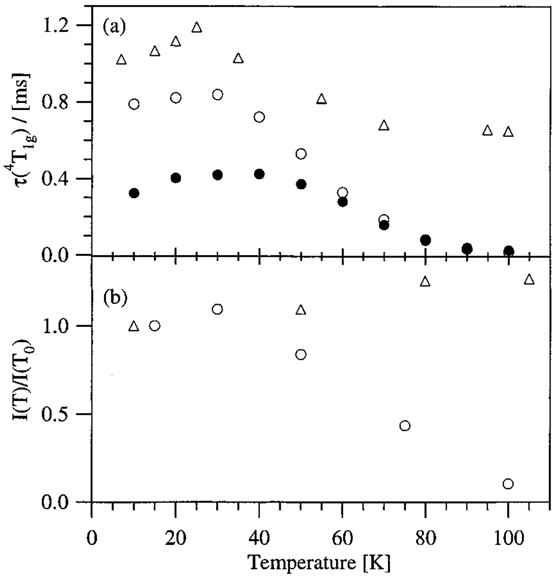

Figure 5. (a) Temperature dependences of the Mn^{2+} $^4T_{1g}$ lifetimes in undoped $CsMnCl_3$ (△) and in 10% Ni^{2+}:$CsMnCl_3$ (○, after Mn^{2+} excitation at 17 599 cm^{-1}; ●, after Ni^{2+} excitation at 12 345 cm^{-1}). (b) Temperature dependences of the relative integrated Mn^{2+} $^4T_{1g} \rightarrow {}^6A_{1g}$ emission intensities in undoped $CsMnCl_3$ (△) and in 10% Ni^{2+}:$CsMnCl_3$ (○) after Mn^{2+} excitation at 17 599 cm^{-1}.

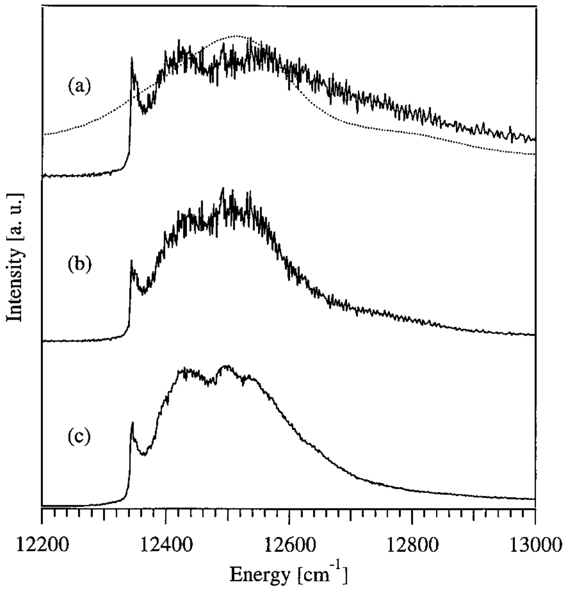

Figure 6. (a) 15 K $^3A_{2g} \rightarrow {}^1E_g$ ground-state absorption (GSA) spectrum (dotted line) and 15 K $^3T_{2g} \rightarrow {}^1T_{2g}$ excited-state excitation (ESE) of 0.1% Ni^{2+}:$CsCdCl_3$ (solid line). In the ESE experiment a Ti:sapphire laser (typical power, 100 mW) was used to provide a high $^3T_{2g}$ population by pumping into the $^3T_{1g}$ (^3F) absorption at 11 000 cm^{-1}. $^1T_{2g} \rightarrow {}^3A_{2g}$ emission at 16 500 cm^{-1} was monitored as a function of wavelength of a second probe Ti:sapphire laser (typical power, 2 mW) (b) Calculated product of the GSA and ESE line shape functions from (a). (c) Experimental 15 K upconversion luminescence excitation spectrum monitoring Ni^{2+} $^1T_{2g} \rightarrow {}^3A_{2g}$ emission at 16 500 cm^{-1}.

The upper half of Figure 5 shows the temperature dependence of the Mn^{2+} $^4T_{1g}$ lifetimes in undoped $CsMnCl_3$ (open triangles) and in 10% Ni^{2+}-doped $CsMnCl_3$ (open circles) after Mn^{2+} excitation at 17 599 cm^{-1}. The full circles represent the temperature-dependent Mn^{2+} $^4T_{1g}$ lifetimes in the same 10% Ni^{2+}:$CsMnCl_3$ crystal after Ni^{2+} excitation at 12 345 cm^{-1}. In the lower half of Figure 5 the integrated Mn^{2+} $^4T_{1g} \rightarrow {}^6A_{1g}$ emission intensitites of undoped $CsMnCl_3$ (open triangles) and of 10% Ni^{2+}:$CsMnCl_3$ (open circles) after Mn^{2+} $^4T_{1g}$ excitation at 17 599 cm^{-1} are plotted against temperature.

Figure 6 shows spectroscopic data of Ni^{2+}:$CsCdCl_3$. Figure 6a shows the 15 K Ni^{2+} $^3A_{2g} \rightarrow {}^1E_g$ ground-state absorption (GSA) spectrum (dotted line) together with the Ni^{2+} $^3T_{2g} \rightarrow {}^1T_{2g}$ excited-state excitation (ESE) spectrum at 15 K (full line). In the ESE experiment the Ni^{2+} $^1T_{2g} \rightarrow {}^3A_{2g}$ emission was monitored at 16 500 cm^{-1}. One Ti:sapphire laser was used to provide a high $^3T_{2g}$ population by pumping into the $^3T_{1g}$

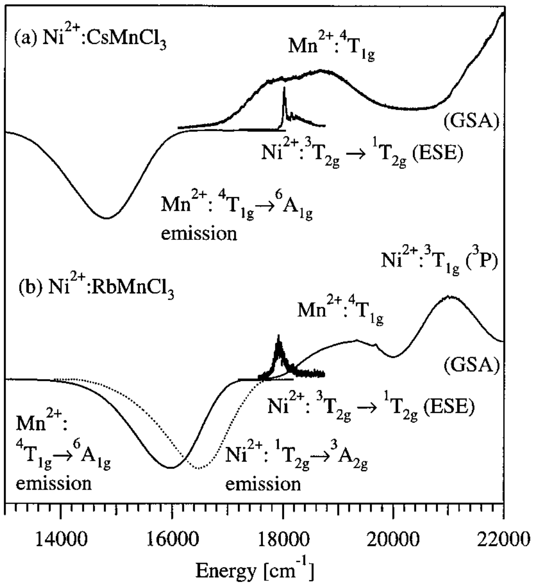

Figure 7. (a) 15 K GSA spectrum of 10% Ni^{2+}:$CsMnCl_3$ in the spectral region of the Mn^{2+} $^4T_{1g}$, $^4T_{2g}$ with the Ni^{2+} $^3T_{2g} \rightarrow {}^1T_{2g}$ ESE spectrum shifted by the energy of the Ni^{2+} $^3T_{2g}$ origin (5660 cm^{-1}), to show the absolute energy of the Ni^{2+} $^1T_{2g}$ excited state with respect to the $^3A_{2g}$ ground state. The Mn^{2+} $^4T_{1g} \rightarrow {}^6A_{1g}$ emission spectrum (excited at 17 599 cm^{-1}) is shown upside down. (b) 15 K GSA spectrum of 10% Ni^{2+}:$RbMnCl_3$ in the spectral region of the Mn^{2+} $^6A_{1g} \rightarrow {}^4T_{1g}$ and Ni^{2+} $^3A_{2g} \rightarrow {}^3T_{1g}$ (^3P) transitions together with the Ni^{2+} $^3T_{2g} \rightarrow {}^1T_{2g}$ ESE spectrum shifted by the energy of the $^3T_{2g}$ origin (5551 cm^{-1}). The 15 K Mn^{2+} $^4T_{1g} \rightarrow {}^6A_{1g}$ and Ni^{2+} $^1T_{2g} \rightarrow {}^3A_{2g}$ emission spectra (excited at 19 436 and 12 345 cm^{-1}, respectively) are shown upside down. The intensities of the GSA and ESE spectra are not comparable.

absorption band at 11 000 cm^{-1}. A second Ti:sapphire laser was used to probe the $^3T_{2g} \rightarrow {}^1T_{2g}$ excited-state absorption transition. The laser powers were around 100 mW for the pump and less than 2 mW for the probe laser. Figure 6b shows the calculated product of the GSA and ESE line shape functions from Figure 6a. Figure 6c presents the experimental 15 K one-color upconversion luminescence excitation spectrum monitoring $^1T_{2g} \rightarrow {}^3A_{2g}$ emission of Ni^{2+} at 16 500 cm^{-1}.

Figure 7a presents data collected on a 10% Ni^{2+}:$CsMnCl_3$ crystal at 15 K. Shown are the GSA spectrum in the spectral region of the Ni^{2+} $^1T_{2g}$, $^1A_{1g}$, and $^3T_{1g}$ (^3P) and the Mn^{2+} $^4T_{1g}$ and $^4T_{2g}$ excited states, the Ni^{2+} $^3T_{2g} \rightarrow {}^1T_{2g}$ ESE spectrum shifted by the energy of the Ni^{2+} $^3T_{2g}$ origin (5660 cm^{-1}), and the Mn^{2+} $^4T_{1g} \rightarrow {}^6A_{1g}$ emission spectrum excited at 17 599 cm^{-1} (upside down). In Figure 7b analogous data measured at 15 K on a 10% Ni^{2+}:$RbMnCl_3$ crystal are presented. The GSA spectrum in the Ni^{2+} $^1T_{2g}$, $^1A_{1g}$, and $^3T_{1g}$ (^3P) and the Mn^{2+} $^4T_{1g}$ and $^4T_{2g}$ energy region and the Ni^{2+} $^3T_{2g} \rightarrow {}^1T_{2g}$ ESE spectrum shifted by the energy of the Ni^{2+} $^3T_{2g}$ origin (5551 cm^{-1}). The 15 K Mn^{2+} $^4T_{1g} \rightarrow {}^6A_{1g}$ downconversion emission spectrum excited at 19 436 cm^{-1} (full line), and the 15 K Ni^{2+} $^1T_{2g} \rightarrow {}^3A_{2g}$ upconversion emission spectrum excited at 12 345 cm^{-1} (dashed line) are shown upside down.

5. Analysis and Discussion

A. Exchange-Enhanced ^1E_g Excitation in Ni^{2+}:$RbMnCl_3$. In diamagnetic host lattices such as $CsCdCl_3$ the spin-forbidden Ni^{2+} transitions from the $^3A_{2g}$ ground state to the ^1E_g, $^1A_{1g}$, and $^1T_{2g}$ excited states gain their intensity via spin−orbit coupling to energetically close-lying spin-allowed d−d transitions (Figure 2a). In magnetic hosts such as $CsMnCl_3$ and $RbMnCl_3$ there is an additional intensity-gaining mechanism for formally spin-forbidden transitions, an intensity mechanism resulting from exchange interactions between the metal centers.[22] Because of this mechanism, the absorption bands of concentrated Mn^{2+} compounds are more intense than those of dilute crystals containing isolated Mn^{2+} ions.[23] It has been demonstrated that the exchange interactions between unlike metal ions are usually stronger than those between like ions.[24,25] Ni^{2+}−Mn^{2+} exchange interactions may therefore lead to an exchange enhancement of the spin-forbidden $^3A_{2g} \rightarrow {}^1E_g$, $^1A_{1g}$, and $^1T_{2g}$ transitions in the absorption spectra of Ni^{2+}:$CsMnCl_3$ and Ni^{2+}:$RbMnCl_3$. However, in these lattices the latter two transitions are obscured by the Mn^{2+} $^6A_{1g} \rightarrow {}^4T_{1g}$ absorption bands. Therefore, we focus on the Ni^{2+} $^3A_{2g} \rightarrow {}^1E_g$ transition. The integrated intensity of this transition is larger in Ni^{2+}:$CsMnCl_3$ than in Ni^{2+}:$CsCdCl_3$ by approximately a factor of 5 (Figure 2a,b). Because of the stronger ligand field in Ni^{2+}:$CsMnCl_3$ relative to Ni^{2+}:$CsCdCl_3$, the $^3T_{1g}$ (^3F) and the ^1E_g excited states are energetically closer to each other in Ni^{2+}:$CsMnCl_3$ than in Ni^{2+}:$CsCdCl_3$ by approximately 15%. This leads to a stronger spin−orbit interaction of the $^3T_{1g}$ (^3F) and ^1E_g excited states in Ni^{2+}:$CsMnCl_3$ than in Ni^{2+}:$CsCdCl_3$, which manifests itself in a weak progression pattern on the high-energy side of the ^1E_g absorption band of Ni^{2+}:$CsMnCl_3$. It indicates that this whole absorption band has a mixed singlet−triplet character, similar to the situation in Ni^{2+}:$CsMgCl_3$.[26] The absorption spectrum of Ni^{2+} in $CsMgCl_3$ is qualitatively and quantitatively very similar to the absorption spectrum of Ni^{2+}:$CsMnCl_3$.[26,27] We therefore conclude that the enhanced ^1E_g absorption intensity in Ni^{2+}:$CsMnCl_3$ (Figure 2b) relative to Ni^{2+}:$CsCdCl_3$ (Figure 2a) is mainly due to stronger spin−orbit interaction of the $^3T_{1g}$ (^3F) and the ^1E_g excited states in the former.

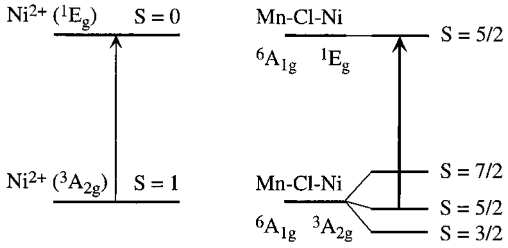

Figure 8. Schematic energy levels and spin quantum numbers of the Ni^{2+}-centered $^3A_{2g} \rightarrow {}^1E_g$ transition for (a) an isolated Ni^{2+} ion in $CsCdCl_3$ and (b) a Ni^{2+}−Mn^{2+} pair in Ni^{2+}:$RbMnCl_3$.

A comparison of the Ni^{2+}:$CsCdCl_3$ and Ni^{2+}:$RbMnCl_3$ absorption spectra (Figure 2a,c) shows that the energetic separation of the $^3T_{1g}$ (^3F) and ^1E_g exicted states is similar in both compounds. Therefore, spin−orbit coupling cannot account for the very pronounced intensity enhancement of the ^1E_g absorption band in Ni^{2+}:$RbMnCl_3$. We conclude that the $^3A_{2g} \rightarrow {}^1E_g$ transition in Ni^{2+}:$RbMnCl_3$ is enhanced by Ni^{2+}−Mn^{2+} exchange interactions. A simple Ni^{2+}−Mn^{2+} dimer picture illustrates the principle of this exchange-induced intensity enhancement, the so-called Tanabe mechanism[23] (see Figure 8). The dimer ground state is [Ni^{2+}($^3A_{2g}$), Mn^{2+}($^6A_{1g}$)] and therefore has dimer spin levels with $S_{\mathrm{dimer}} = {}^3/_2, {}^5/_2, {}^7/_2$. The

---

[22] McCarthy, P. J.; Güdel, H. U. *Coord. Chem. Rev.* **1988**, *88*, 69−131 and references therein.
[23] Ferguson, J.; Guggenheim, H. J.; Tanabe, Y. *J. Phys. Soc. Jpn.* **1966**, *21*, 692−704.
[24] Ferguson, J.; Guggenheim, H. J.; Tanabe, Y. *J. Chem. Phys.* **1966**, *45*, 1134−1141.
[25] Gondaira, K.; Tanabe, Y. *J. Phys. Soc. Jpn.* **1966**, *21*, 1527−1548.
[26] Buissière, G.; Reber, C. *J. Am. Chem. Soc.* **1998**, *120*, 6306−6315.
[27] McPherson, G. L.; Stucky, G. D. *J. Chem. Phys.* **1972**, *57*, 3780−3786.

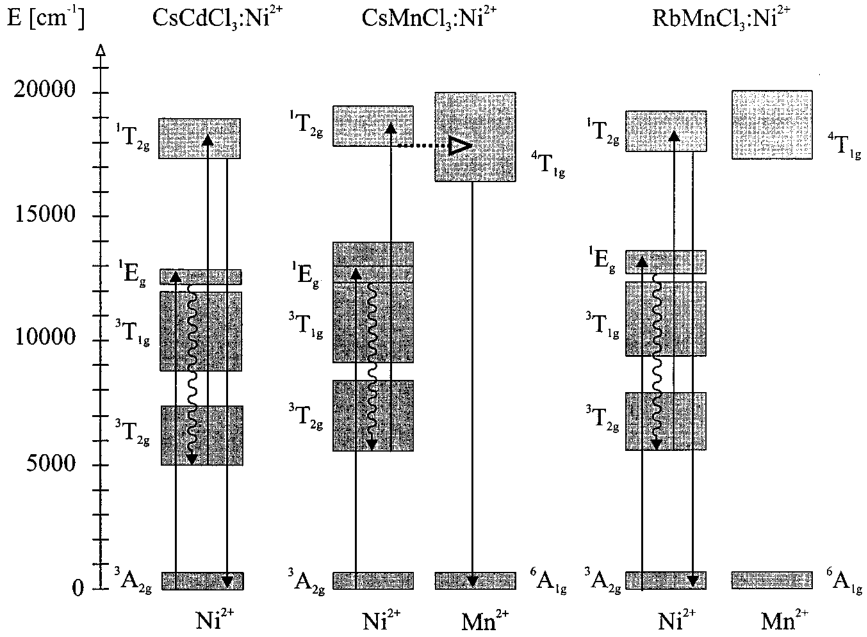

Figure 9. Summary of the near-infrared to visible upconversion processes in Ni^{2+}:$CsCdCl_3$, Ni^{2+}:$CsMnCl_3$, and Ni^{2+}:$RbMnCl_3$. The solid arrows represent radiative processes of GSA, ESA, and luminescence. The curly arrows indicate nonradiative multiphonon relaxation processes, and the dashed arrow represents an energy-transfer process.

Ni^{2+}-centered ^1E_g excited state has $S_{Ni} = 0$, and therefore, the corresponding [Ni^{2+}(^1E_g), Mn^{2+}($^6A_{1g}$)] dimer excited state has only one $S_{dimer} = {}^5/_2$ spin level. Thus, there is a formally spin-allowed $S_{dimer} = {}^5/_2 \rightarrow {}^5/_2$ transition that dominates the $^3A_{2g} \rightarrow {}^1E_g$ oscillator strength in the Ni^{2+}:$RbMnCl_3$ absorption spectrum. This transition is thermally activated with an intensity maximum around 50 K, in agreement with the fact that $S_{dimer} = {}^5/_2$ is not the ground state in Figure 8. Above this temperature the $^3A_{2g} \rightarrow {}^1E_g$ oscillator strength decreases again and reaches a value at 300 K that is about 10% lower than that at 50 K. By contrast, the $^3A_{2g} \rightarrow {}^1E_g$ oscillator strengths in Ni^{2+}:$CsMnCl_3$ and Ni^{2+}:$CsCdCl_3$ increase with increasing temperature steadily up to 300 K. In both these materials the respective oscillator strength is approximately 30% larger at 300 K than at 15 K. The difference in the temperature dependence of the $^3A_{2g} \rightarrow {}^1E_g$ oscillator strength in Ni^{2+}:$RbMnCl_3$ and Ni^{2+}:$CsMnCl_3$ is therefore another indication that the intensity-gain mechanism for that transition is different in these two compounds, i.e., $Ni^{2+}-Mn^{2+}$ exchange interaction in the case of Ni^{2+}:$RbMnCl_3$ leading to an intensity maximum at a specific temperature and spin−orbit interaction in the case of Ni^{2+}:$CsMnCl_3$ leading to a steady increase of the absorption oscillator strength with increasing temperature. The simple dimer picture for Ni^{2+}:$RbMnCl_3$ thus provides a satisfactory qualitative explanation of the observed $^3A_{2g} \rightarrow {}^1E_g$ absorption temperature dependence, but it is not capable of modeling it quantitatively. The real situation in Ni^{2+}:$RbMnCl_3$ is more complicated. Each Ni^{2+} ion has four nearest Mn^{2+} neighbors instead of one. In addition the $RbMnCl_3$ lattice is antiferromagnetically ordered below 94 K.[19]

It is a characteristic of the Tanabe intensity mechanism that pure spin−flip transitions involving no changes in electron orbital occupancies are influenced most strongly by exchange interactions, while spin-allowed transitions essentially stay unaffected. Spin-forbidden transitions involving an orbital promotion represent an intermediate case. These trends are observed in Figure 2c, where the pure spin−flip $^3A_{2g} \rightarrow {}^1E_g$ transition shows by far the largest exchange enhancement. From the fact that this $^3A_{2g} \rightarrow {}^1E_g$ transition is exchange-enhanced in Ni^{2+}:$RbMnCl_3$ but not in Ni^{2+}:$CsMnCl_3$ (see above) we conclude that the $Ni^{2+}-Mn^{2+}$ exchange interaction is stronger in Ni^{2+}:$RbMnCl_3$ than in Ni^{2+}:$CsMnCl_3$. The spin density of the Ni^{2+} d^8 ion is located in the e_g set of d orbitals and thus has a σ-type interaction with Cl^- ligand orbitals. Consequently, the dominant $Ni^{2+}-Mn^{2+}$ exchange interactions occur via a σ-superexchange pathway, which is most efficient for a 180° $Ni^{2+}-Cl^{-}-Mn^{2+}$ bridge,[28,29] i.e., corner-sharing octahedral units. As mentioned in section 2, it is reasonable to assume that the Ni^{2+} dopant ions predominately occupy one of two crystallographically distinct Mn^{2+} sites in both $RbMnCl_3$ and $CsMnCl_3$. In Ni^{2+}:$RbMnCl_3$ the Ni^{2+} dopant ions occupy the C_{3v} site, and consequently, corner-sharing $Ni^{2+}-Cl^{-}-Mn^{2+}$ bridges exist (see Figure 1). In Ni^{2+}:$CsMnCl_3$ we have no direct EPR information on the identity of the Ni^{2+} site. Because we observe no exchange enhancement of the ^1E_g excitation, we conclude that Ni^{2+} occupies the D_{3d} site in this lattice (see Figure 1). This site is sharing faces of the two neighboring Mn^{2+} octahedra, and thus, there is no efficient 180° $Ni^{2+}-Cl^{-}-Mn^{2+}$ exchange pathway.

B. Downconversion Luminescence. Dynamics and Temperature Dependences. 1. Ni^{2+} $^3T_{2g}$ First Excited-State Emission. Figure 9 presents the Ni^{2+} energy level schemes for Ni^{2+}:$CsCdCl_3$, Ni^{2+}:$CsMnCl_3$, and Ni^{2+}:$RbMnCl_3$. In all three compounds excitation with a Ti:sapphire laser into the Ni^{2+} $^3T_{1g}$ (^3F) and ^1E_g excited states leads to rapid (typically within picoseconds) nonradiative multiphonon relaxation to the $^3T_{2g}$ first excited state. From there near-infrared $^3T_{2g} \rightarrow {}^3A_{2g}$ emission occurs at temperatures below 200 K (spectra not shown). In the 15−100 K temperature range the integrated $^3T_{2g} \rightarrow {}^3A_{2g}$ emission intensity is nearly constant in all three compounds considered in this study (data not shown), and we conclude that nonradiative relaxation processes can be neglected below 100 K. The 15 K $^3T_{2g}$ lifetimes in 0.1% Ni^{2+}:$CsCdCl_3$, 10% Ni^{2+}:$CsMnCl_3$, and 10% Ni^{2+}:$RbMnCl_3$ are 7.8, 6.8, and 5.8 ms, respectively. The temperature dependences of these lifetimes

---

(28) Ferguson, J.; Guggenheim, H. J.; Tanabe, Y. *Phys. Rev. Lett.* **1965**, *14*, 737−738.

(29) Ferguson, J.; Guggenheim, H. J.; Tanabe, Y. *Phys. Rev.* **1967**, *161*, 207−212.

in the 15−100 K temperature range shown in Figure 3 can be fitted with the following equation:[30]

$$\tau_{\mathrm{rad}}(T) = \tau_{\mathrm{rad}}(T_0)\left[\coth\left(\frac{\nu_{\mathrm{eff}}}{2kT}\right)\right]^{-1} \qquad (1)$$

Equation 1 describes the temperature dependence of the radiative lifetime τ_{rad} as resulting from an increased $^3A_{2g} \rightarrow {}^3T_{2g}$ absorption oscillator strength upon warming due to thermally induced vibronic intensity. ν_{eff} is a weighted average of the ungerade enabling modes in the Herzberg−Teller mechanism. Reasonable fits with eq 1 to the experimental $^3T_{2g}$ lifetime data between 15 and 100 K are obtained with the following fit parameters: $\nu_{\mathrm{eff}} = 130 \pm 10$ cm^{-1} (Ni^{2+}:CsCdCl$_3$), 101 ± 10 cm^{-1} (Ni^{2+}:CsMnCl$_3$), and 90 ± 10 cm^{-1} (Ni^{2+}:RbMnCl$_3$).

For each of the three crystals considered here, there is a temperature above 100 K where nonradiative multiphonon relaxation becomes important, causing a steep decrease in both the $^3T_{2g} \rightarrow {}^3A_{2g}$ emission intensity and the $^3T_{2g}$ lifetime (data not shown). These temperatures are 175 ± 5 K in 0.1% Ni^{2+}:CsCdCl$_3$, 150 ± 5 K in 10% Ni^{2+}:CsMnCl$_3$, and 110 ± 5 K in 10% Ni^{2+}:RbMnCl$_3$.

2. Ni^{2+}/Mn^{2+} Emission in the Visible Spectral Region. a. Ni^{2+}:CsCdCl$_3$. A close inspection of the Ni^{2+}:CsCdCl$_3$ absorption spectrum (Figure 2a) reveals that both the energy gap between the Ni^{2+} $^3T_{2g}$ first excited state and the $^3A_{2g}$ ground state and the energy gap between the $^1T_{2g}$ and ^1E_g higher excited states are about 5000 cm^{-1}. It is therefore not too surprising to find radiative emission of Ni^{2+} not only from the $^3T_{2g}$ first excited state but also from the $^1T_{2g}$ higher excited state. From there, transitions to all lower-lying levels are observed at cryogenic temperatures. Shown in Figure 4a are the three spin-forbidden transitions to the $^3A_{2g}$, $^3T_{2g}$, and $^3T_{1g}$ (^{3}F) states. In 0.1% Ni^{2+}:CsCdCl$_3$ the $^1T_{2g}$ lifetime is 85 μs at 15 K. With increasing temperature, this lifetime drops sharply. This lifetime reduction is accompanied by a corresponding decrease in $^1T_{2g}$ emission intensity (data not shown). This indicates that nonradiative multiphonon relaxation processes play a significant role down to the lowest temperatures. At 300 K, $^1T_{2g}$ emission is completely quenched. A comparison of the 15 K Ni^{2+}:CsCdCl$_3$ emission (Figure 4a) and absorption spectra (Figure 2a) reveals energy regions where emission and absorption bands overlap. This enables nonradiative cross-relaxation processes, particularly in concentrated Ni^{2+} systems, at the expense of $^1T_{2g}$ luminescence. To obtain a high quantum efficiency of visible $^1T_{2g} \rightarrow {}^3A_{2g}$ emission, the Ni^{2+} dopant concentration therefore has to be very low.[31]

b. Ni^{2+}:CsMnCl$_3$. In Ni^{2+}:CsMnCl$_3$, excitation with 17 599 cm^{-1} photons exclusively leads to $^4T_{1g} \rightarrow {}^6A_{1g}$ luminescence of Mn^{2+} in the visible spectral region as shown in Figure 4b. It will be demonstrated in section 5.C that the origin of the Ni^{2+} $^1T_{2g}$ excited state is around 17 800 cm^{-1}, more than 1300 cm^{-1} above the origin of the Mn^{2+} $^4T_{1g}$ first excited state in this material.[21] Excitation at 17 599 cm^{-1} therefore only excites Mn^{2+} ions. At 10 K the $^4T_{1g}$ lifetime in 10% Ni^{2+}:CsMnCl$_3$ is 0.79 ms (Figure 5a), compared to 1.02 ms in undoped CsMnCl$_3$. Partial Mn^{2+} → Ni^{2+} energy transfer in 10% Ni^{2+}:CsMnCl$_3$ and subsequent fast relaxation on the Ni^{2+} center cannot account for this shortening for energetic reasons (see above). We ascribe it to the following two effects. First, the relatively high Ni^{2+} dopant concentration will cause changes in the Mn^{2+} crystal field environment and may therefore lead to a reduction of the Mn^{2+} $^4T_{1g}$ lifetime. Second, there is evidence for an additional Mn^{2+} $^4T_{1g}$ depopulation process in Ni^{2+}:CsMnCl$_3$ that does not exist in undoped CsMnCl$_3$. After pure $^4T_{1g}$ excitation of Mn^{2+} at 17 599 cm^{-1}, Ni^{2+} $^3T_{2g} \rightarrow {}^3A_{2g}$ near-infrared emission is observed, even at 15 K. A comparison of the 10% Ni^{2+}:CsMnCl$_3$ absorption (Figure 2b) and emission spectra (Figure 4b) indicates how this Mn^{2+} → Ni^{2+} energy transfer occurs. There is some spectral overlap of Mn^{2+} $^4T_{1g} \rightarrow {}^6A_{1g}$ emission with Ni^{2+} $^3A_{2g} \rightarrow {}^3T_{1g}$, ^1E_g absorption between 12 700 and 14 000 cm^{-1}. Consequently, Mn^{2+} $^4T_{1g}$, Ni^{2+} $^3A_{2g}$ → Mn^{2+} $^6A_{1g}$, Ni^{2+} $^3T_{1g}/^1E_g$ cross-relaxation can take place and thus lead to a shortening of the Mn^{2+} $^4T_{1g}$ lifetime in 10% Ni^{2+}:CsMnCl$_3$ relative to that of the undoped CsMnCl$_3$.

The temperature dependence of the $^4T_{1g}$ lifetime between 7 and 100 K in undoped CsMnCl$_3$ (open triangles in Figure 5a) has been explained as follows.[21] The $^4T_{1g}$ origin of the D_{3d} Mn^{2+} ions is energetically lower than the $^4T_{1g}$ origin of the C_{3v} Mn^{2+} ions. As a consequence, there is a unidirectional C_{3v} Mn^{2+} → D_{3d} Mn^{2+} energy transfer at the lowest temperatures. This process is thermally activated and becomes more efficent between 10 and 30 K, causing an increase of the $^4T_{1g}$ lifetime due to the longer radiative lifetime of the centrosymmetric D_{3d} site, relative to the noncentrosymmetric C_{3v} site. Above 30 K, D_{3d} Mn^{2+} → C_{3v} Mn^{2+} back energy transfer becomes important, resulting in a decrease of the $^4T_{1g}$ lifetime. Up to 100 K there is no reduction of the integrated $^4T_{1g} \rightarrow {}^6A_{1g}$ emission intensity in undoped CsMnCl$_3$ (open triangles in Figure 5b), indicating that in this sample nonradiative $^4T_{1g}$ depopulation is unimportant between 10 and 100 K.

As shown in Figure 5, in 10% Ni^{2+}:CsMnCl$_3$ the temperature dependence of the Mn^{2+} $^4T_{1g}$ lifetime and the Mn^{2+} $^4T_{1g} \rightarrow {}^6A_{1g}$ integrated emission intensity is analogous to that of undoped CsMnCl$_3$ only between 10 and 30 K. Above 30 K the decrease of the Mn^{2+} $^4T_{1g}$ lifetime is accompanied by a decrease of the Mn^{2+} $^4T_{1g} \rightarrow {}^6A_{1g}$ emission intensity. At 100 K, the Mn^{2+} emission is almost completely quenched in 10% Ni^{2+}:CsMnCl$_3$. We ascribe this to an increased Mn^{2+} $^4T_{1g}$, Ni^{2+} $^3A_{2g}$ → Mn^{2+} $^6A_{1g}$, Ni^{2+} $^3T_{1g}/^1E_g$ cross-relaxation efficiency as the temperature is raised.

c. Ni^{2+}:RbMnCl$_3$. At 10 K, excitation into the Ni^{2+} $^3T_{1g}$ (^{3}P) absorption band of 10% Ni^{2+}:RbMnCl$_3$ at 20 986 cm^{-1} leads to the same Ni^{2+} emission transitions as observed in 10% Ni^{2+}:CsCdCl$_3$ (Figure 4) but with completely different relative intensities. As expected from the similarity of host lattices, the transitions occur at a very similar energy in the emission spectra of both compounds. The broad emission feature around 16 000 cm^{-1} in the Ni^{2+}:RbMnCl$_3$ spectrum consists of overlapping Ni^{2+} $^1T_{2g} \rightarrow {}^3A_{2g}$ (90%) and Mn^{2+} $^4T_{1g} \rightarrow {}^6A_{1g}$ (10%) luminescence transitions due to a coexcitation of both ions at 20 986 cm^{-1}. Selective Ni^{2+} excitation in the near-infrared (see section 5.C) results in a pure Ni^{2+} $^1T_{2g} \rightarrow {}^3A_{2g}$ emission band with an origin around 17 800 cm^{-1} as shown in Figure 7b (dotted trace). On the other hand, selective Mn^{2+} $^4T_{1g}$ excitation at 19 436 cm^{-1} is followed by pure Mn^{2+} $^4T_{1g} \rightarrow {}^6A_{1g}$ emission (Figure 7b, full trace). As in the undoped RbMnCl$_3$, the origin of this Mn^{2+} emission is around 17 500 cm^{-1} and the $^4T_{1g}$ lifetime is about 1 ms (lifetime data not shown). Consequently, the origin of the Ni^{2+} $^1T_{2g}$ excited state lies approximately 300 cm^{-1} above the origin of the Mn^{2+} $^4T_{1g}$ excited state. The energy transfer from the $^1T_{2g}$ of Ni^{2+} to the $^4T_{1g}$ of Mn^{2+} is not quantitative at 15 K because there are very fast $^1T_{2g}$ relaxation processes that compete with Ni^{2+} → Mn^{2+} energy transfer in 10% Ni^{2+}:RbMnCl$_3$. Two of these are independent of the Mn

---

(30) Ballhausen, C. J. *Introduction to Ligand Field Theory*; McGraw-Hill: New York, 1962.

(31) May, P. S.; Güdel, H. U. *Chem. Phys. Lett.* **1989**, *164*, 612−616.

host lattice and have their origin in the high Ni^{2+} concentration. It has been demonstrated in previous studies on Ni^{2+}-doped $CsCdCl_3$ that the following cross-relaxation processes become important at Ni^{2+} concentrations above 0.1%: $^1T_{2g}$, $^3A_{2g} \rightarrow {}^3T_{2g}$, $^3T_{1g}$ (^3F) and $^1T_{2g}$, $^3A_{2g} \rightarrow {}^3T_{1g}$ (^3F), $^3T_{1g}$ (^3F).[31,32] Another process is due to the efficient $Ni^{2+}-Cl^{-}-Mn^{2+}$ exchange interaction in this system. The $^1T_{2g} \rightarrow {}^3A_{2g}$ transition is hardly affected by exchange interaction (section 5.A); therefore, the emission spectra of 10% Ni^{2+}:$CsCdCl_3$ and 10% Ni^{2+}:$RbMnCl_3$ are scaled to an equal integrated Ni^{2+} $^1T_{2g} \rightarrow {}^3A_{2g}$ emission intensity. Comparison of the respective emission spectra (Figure 4) shows that the $^1T_{2g} \rightarrow {}^3T_{2g}$ transition around 12 000 cm^{-1} has an increased oscillator strength by about an order of magnitude in Ni^{2+}:$RbMnCl_3$ compared to that in Ni^{2+}:$CsCdCl_3$. This leads to a reduction of the $^1T_{2g}$ lifetime by a factor of 4 in the magnetic host lattice. In concert, these three processes prevent an efficient energy transfer (ET) from $^1T_{2g}$ on Ni^{2+} to $^4T_{1g}$ on Mn^{2+} at 15 K. At higher temperatures this ET becomes more competitive because of better spectral overlap, and we observe a slow decay component due to Mn^{2+} $^4T_{1g} \rightarrow {}^6A_{1g}$ superimposed on the fast Ni^{2+} $^1T_{2g}$ emission in the lifetime of the broad luminescence band measured at 16 500 cm^{-1}. The two emissions overlap, but do not coincide, which leads to a broadening of the band at elevated temperatures (data not shown).

C. Upconversion and Relaxation Mechanisms. Near-infrared excitation around 12 500 cm^{-1} into ^1E_g of a 10% Ni^{2+}:$CsCdCl_3$ crystal at 15 K leads to an upconversion luminescence spectrum that is identical to the downconversion luminescence spectrum obtained after excitation into the Ni^{2+} $^3T_{1g}$ (^3P) excited state (Figure 4a). The same is true for 10% Ni^{2+}:$RbMnCl_3$ with the only small difference that the upconversion luminescence spectrum is a pure Ni^{2+} spectrum, whereas the spectrum excited at 20 986 cm^{-1} (Figure 4c) contains a small amount of Mn^{2+} $^4T_{1g}$ emission. Ni^{2+}:$CsMnCl_3$ shows contrasting behavior; Ni^{2+} ^1E_g excitation in the near-infrared exclusively leads to visible Mn^{2+} $^4T_{1g} \rightarrow {}^6A_{1g}$ emission, the same as observed after direct Mn^{2+} excitation (Figure 4b).

From this behavior we derive the excitation and relaxation schemes in Figure 9 for the three systems. Excitation in the near-infrared into ^1E_g is followed by fast multiphonon relaxation to $^3T_{2g}$ and upconversion to $^1T_{2g}$ in all the three systems. Luminescence from $^1T_{2g}$ into the various lower-lying states of Ni^{2+} is then observed below 100 K in the $CsCdCl_3$ and $RbMnCl_3$ hosts, whereas in 10% Ni^{2+}:$CsMnCl_3$ the $^1T_{2g}$ excitation of Ni^{2+} is transferred to $^4T_{1g}$ of Mn^{2+}, from which emission takes place.

What is the mechanism of the upconversion process? From a comparison of the spectra in Figure 6 we can answer this question for 0.1% Ni^{2+}:$CsCdCl_3$ at 15 K, and this answer can then be generalized for the other systems. First we note that the ground-state absorption (GSA) spectrum (dotted line in Figure 6a) is not identical with the one-color upconversion excitation spectrum (Figure 6c). The latter shows additional structure and a sharp feature at about 12 350 cm^{-1}. These same features are also observed in the $^3T_{2g} \rightarrow {}^1T_{2g}$ excited-state excitation (ESE) spectrum shown in Figure 6a (full line). It follows that the sharp features in the one-color upconversion excitation spectrum of Figure 6c are due to a $^3T_{2g} \rightarrow {}^1T_{2g}$ excited-state absorption (ESA) process. We conclude that upconversion occurs by a sequence of $^3A_{2g} \rightarrow {}^1E_g$ (GSA) and $^3T_{2g} \rightarrow {}^1T_{2g}$ (ESA) steps.

In a pure GSA/ESA upconversion mechanism the one-color upconversion excitation spectrum is given by the product of the GSA and ESA line shape functions.[33] This product, obtained from multiplication of the two spectra in Figure 6a, is shown in Figure 6b. Its agreement with the one-color upconversion excitation spectrum of Figure 6c is very good. In 10% Ni^{2+}:$CsMnCl_3$ the agreement is almost equally good, whereas in 10% Ni^{2+}:$RbMnCl_3$ it is slightly worse (data not shown). We conclude that in all three systems GSA/ESA is the predominant upconversion mechanism. The alternative energy-transfer upconversion (ETU) mechanism would exhibit a different signature from that observed in Figure 6. In addition, an ETU mechanism can also be ruled out on energetic grounds.

The $^3T_{2g} \rightarrow {}^1T_{2g}$ ESE spectra at 15 K of 10% Ni^{2+}:$CsMnCl_3$ and 10% Ni^{2+}:$RbMnCl_3$ are shown in Figure 7. They are shifted to higher energies by 5660 and 5551 cm^{-1}, respectively, i.e., by the energies of the $^3T_{2g}$ origins, to show the absolute energies of the Ni^{2+} $^1T_{2g}$ excited states relative to the $^3A_{2g}$ ground state. The comparison of this ESE spectrum with the GSA spectrum in Figure 7a shows that in 10% Ni^{2+}:$CsMnCl_3$ the Ni^{2+} $^1T_{2g}$ origin lies more than 1300 cm^{-1} above the Mn^{2+} $^4T_{1g}$ origin. Consequently, there is a good spectral overlap for nonradiative Ni^{2+} $^1T_{2g} \rightarrow Mn^{2+}$ $^4T_{1g}$ energy transfer. It has been demonstrated in a previous study that in the $CsMnCl_3$ host there is essentially no $Mn^{2+} \rightarrow Mn^{2+}$ energy migration at 15 K; i.e., the excitation energy is self-trapped in the Mn^{2+} $^4T_{1g}$ excited state.[34] Therefore, in 10% Ni^{2+}:$CsMnCl_3$ at 15 K, after Ni^{2+} near-infrared excitation followed by upconversion and $Ni^{2+} \rightarrow Mn^{2+}$ energy transfer, the excitation stays in proximity to the Ni^{2+} ions. The following cross-relaxation process is thus likely to contribute to the Mn^{2+} $^4T_{1g}$ deactivation: Mn^{2+} $^4T_{1g}$, Ni^{2+} $^3A_{2g} \rightarrow Mn^{2+}$ $^6A_{1g}$, Ni^{2+} $^3T_{1g}/^1E_g$. This explains the different $^4T_{1g}$ lifetimes of 10% Ni^{2+}:$CsMnCl_3$ below 70 K after upconversion excitation via Ni^{2+} (full circles in Figure 5a) and direct excitation of the bulk Mn^{2+} at 17 599 cm^{-1} (open circles in Figure 5a). With the two excitation modes we thus probe different subsets of Mn^{2+} ions in the crystal. At elevated temperatures $Mn^{2+} \rightarrow Mn^{2+}$ energy migration becomes important, and the same value for the Mn^{2+} $^4T_{1g}$ lifetime is obtained above 70 K after both Ni^{2+} excitation in the near-infrared and after direct Mn^{2+} excitation.

A comparison of the GSA and Ni^{2+} $^3T_{2g} \rightarrow {}^1T_{2g}$ ESE spectra of 10% Ni^{2+}:$RbMnCl_3$ at 15 K in Figure 7 shows that in this system the origins of the Ni^{2+} $^1T_{2g}$ and the Mn^{2+} $^4T_{1g}$ excited states are energetically much closer than in 10% Ni^{2+}:$CsMnCl_3$. In the case of 10% Ni^{2+}:$RbMnCl_3$ the energetic separation of the respective origins is better extracted from the Ni^{2+} $^1T_{2g} \rightarrow {}^3A_{2g}$ and Mn^{2+} $^4T_{1g} \rightarrow {}^6A_{1g}$ emission spectra (both shown upside down in Figure 7b). The Ni^{2+} $^1T_{2g}$ origin lies about 300 cm^{-1} above the Mn^{2+} $^4T_{1g}$ origin. The spectral overlap required for Ni^{2+} $^1T_{2g} \rightarrow Mn^{2+}$ $^4T_{1g}$ energy transfer is therefore several orders of magnitude smaller in 10% Ni^{2+}:$RbMnCl_3$ than in 10% Ni^{2+}:$CsMnCl_3$. In particular, as discussed in section 5.B, at 15 K this energy-transfer process is negligible compared to the other processes deactivating $^1T_{2g}$. As a consequence, in contrast to the $CsMnCl_3$ host, no Mn^{2+} emission is observed upon Ni^{2+} upconversion excitation.

D. Effect of Exchange Interactions on Upconversion. We have established a sequence of GSA and ESA steps as the predominant upconversion mechanism in all three chemical systems (see Figure 9). Both the GSA and ESA steps are

---

(32) May, P. S.; Güdel, H. U. *J. Chem. Phys.* **1991**, *95*, 6343−6354.

(33) Pollnau, M.; Gamelin, D. R.; Lüthi, S. R.; Hehlen, M. P.; Güdel, H. U. *Phys. Rev. B* **2000**, *61*, 3337−3346.

(34) Kambli, U.; Güdel, H. U. *Inorg. Chem.* **1984**, *23*, 3479−3486.

formally spin-forbidden triplet to singlet spin−flip transitions and are therefore weak in Ni^{2+}:$CsCdCl_3$. Thus, the whole upconversion process in this compound is relatively inefficent. In 10% Ni^{2+}:$RbMnCl_3$, on the other hand, the single-ion spin selection rules relax due to $Ni^{2+}-Mn^{2+}$ exchange interactions. Specifically, the pure spin−flip $^3A_{2g} \rightarrow {}^1E_g$ and the $^3T_{2g} \rightarrow {}^1T_{2g}$ transitions, corresponding to the GSA and ESA steps in the upconversion mechanism, are exchange-enhanced by factors of 20 and 10, respectively, in 10% Ni^{2+}:$RbMnCl_3$ relative to 10% Ni^{2+}:$CsCdCl_3$. The Ni^{2+} $^3T_{2g}$ first excited state serves as an energy storage reservoir for the second upconversion step (ESA). A long lifetime helps to establish a high population of Ni^{2+} ions that can be upconverted to the $^1T_{2g}$ excited state. Because the $^3A_{2g} \rightarrow {}^3T_{2g}$ transition is spin-allowed, the $Ni^{2+}-Mn^{2+}$ exchange interaction does not affect its oscillator strength. The radiative $^3T_{2g}$ lifetimes in Ni^{2+}:$RbMnCl_3$ ($\tau_{15K} = 5.8$ ms) and in Ni^{2+}:$CsCdCl_3$ ($\tau_{15K} = 7.8$ ms) are therefore about the same. Taking into account that the $^3T_{2g}$ lifetime is a factor of 1.34 shorter in Ni^{2+}:$RbMnCl_3$ than in Ni^{2+}:$CsCdCl_3$, a total enhancement of the upconversion rate by a factor of roughly 150 is calculated for the magnetic lattice.[35] This is compared to an experimentally determined enhancement factor of 80, which was obtained from a comparison of 15 K upconversion luminescence intensities in 10% Ni^{2+}:$CsCdCl_3$ and 10% Ni^{2+}:$RbMnCl_3$ after two-color excitation with one laser in resonance with the GSA maximum and a second laser in resonance with the ESA maximum. Considering the experimental uncertainty of roughly a factor of 4 in this experiment, the calculated and observed enhancement factors agree fairly well.

The comparison of the 10% Ni^{2+}:$RbMnCl_3$ and 10% Ni^{2+}:$CsMnCl_3$ systems demonstrates the importance of the bridging geometry for the $Ni^{2+}-Mn^{2+}$ exchange interaction. It is strongest for a 180° $Ni^{2+}-Cl^{-}-Mn^{2+}$ bridging angle occurring between sites A and B in Ni^{2+}:$RbMnCl_3$ (see Figure 1).

The specialty of 10% Ni^{2+}:$CsMnCl_3$ is the enhanced *visible* luminescence quantum yield after near-infrared excitation (see Figure 4). In 10% Ni^{2+}:$CsCdCl_3$ and 10% Ni^{2+}:$RbMnCl_3$ there are three Ni^{2+} inter-excited-state luminescence transitions in the near-infrared spectral region that compete with the visible $^1T_{2g} \rightarrow {}^3A_{2g}$ upconversion luminescence. This is avoided in Ni^{2+}:$CsMnCl_3$ where the upconverted energy is transferred to Mn^{2+}, which emits exclusively in the visible spectral region. Using the $^1T_{2g}$ emission branching ratio of Ni^{2+}:$CsCdCl_3$ as a basis, we calculate an enhancement of visible upconversion luminescence output in Ni^{2+}:$CsMnCl_3$ relative to Ni^{2+}:$CsCdCl_3$ by roughly a factor of 5 at 15 K. Such a selective enhancement of *visible* upconversion luminescence has no precedent.

In summary, we have established in this study that exchange interactions between transition metal ions can be exploited for the modification of transition metal upconversion properties. We have shown that the combination of transition metal upconversion ions with other emitting (transition metal) ions provides a tool for the tuning of the upconversion luminescence properties. In this sense the present study demonstrates the broader principle of environmental control of transition metal upconversion properties using chemical means. The feasibility of such controlled modifications represents the major advantage of transition metal ion upconversion systems when compared to the lanthanide systems where, because of the shielded nature of the spectroscopically active f orbitals, a controlled tuning of the upconversion properties by means of chemistry is impossible.

Acknowledgment. The authors thank Daniel R. Gamelin for many valuable discussions. This research has been financially supported by the Swiss National Science Foundation.

IC000662P

---

(35) Wenger, O. S.; Gamelin, D. R.; Güdel, H. U. *J. Am. Chem. Soc.* **2000**, *122*, 7408−7409.